

The Environmental Response to Aerosols observed in CCI ECVs (ERACE)



Adam C. Povey
National Centre for Earth Observation
Atmospheric, Oceanic and Planetary Physics
University of Oxford

CCI Living Planet Fellowship Final Report
22 December 2017

Responsible person Adam C. Povey
Contract No. 4000112801/15/I-SBo
Document No. CCI-LPF/ERACE/F-Report-12-2017

Introduction

Aerosols and clouds interact with radiation by various mechanisms and thereby influence the climate. Such interactions were labelled the most uncertain influence on climate change by the most recent report of the Intergovernmental Panel on Climate Change (IPCC, 2014). The two readily interact with each other because an aerosol particle can 'become' a cloud droplet as water condenses onto it (and vice versa). They exist in a dynamic equilibrium driven by thermodynamics. Aerosol that can form cloud droplets are known as cloud condensation nuclei (CCN).

Cloud droplets tend to effectively interact with radiation such that clouds are expected to reflect a substantial amount of sunlight into space, producing a cooling effect on the climate (Dines, 1917). This is known as the cloud radiative effect (CRE) and its magnitude is a function of droplet number and size, with small droplets being more efficient reflectors than large ones (Twomey, 1967). However, the shortwave CRE is irrelevant over bright surfaces, such as snow, as the land would reflect the light in the absence of the cloud. Once droplets freeze, ice nuclei scatter thermal radiation, resulting in a warming effect (Manabe et al., 1964). Hence, changes in the location or properties of cloud can produce positive or negative global radiative effects (as reviewed in Stephens, 2005).

Aerosol particles are less effective at diverting radiation than cloud droplets so, while they will produce a direct cooling effect (Haywood and Shine, 1995), there is significant interest in their influence on a cloud's equilibrium and the resulting change in CRE. These are known as aerosol-cloud interactions (ACI). Various theorised mechanisms are reviewed in Lohmann and Feichter (2005). The most widely confirmed of these, described in Twomey (1977), is the first indirect effect: when CCN are introduced into a cloud with fixed liquid water, the average droplet size decreases. Measuring ACI is broadly a matter of observing the change in some cloud parameter as a function of the aerosol loading and requires global coverage which can only currently be provided by passive imagery.

The aerosol index (AI), a product of AOD and Ångström exponent, is widely used as a proxy for CCN (Liu and Li, 2014; Nakajima et al., 2001). There is increasing discussion about how representative it is (Stier, 2016) as there are variables that alter both cloud properties and AOD, such as humidity. A change in such a 'confounding variable' could be mistaken for an ACI (Gryspeerd et al., 2014). Using a more direct measure of CCN would be preferable (Gryspeerd et al., 2017). While satellite retrievals have been proposed (Rosenfeld et al., 2012), they have yet to be applied or validated globally in a systematic fashion. The scales over which data is considered can also produce erroneous ACI due to spatial variations (McComiskey and Feingold, 2012; Grandey and Stier, 2010).

It is therefore necessary to estimate the aerosol loading within cloud. Nearby aerosol properties can be useful as they are spatially correlated over some distance (usually cited as 50 km from Anderson et al. (2003) though Shinozuka and Redemann (2011) showed that it can vary significantly). The most common method is pre-averaging (e.g. Christensen et al., 2016; Quaas et al., 2008), whereby data is averaged over regions sufficiently large to observe both aerosol and cloud, typically daily $1^\circ \times 1^\circ$. Process studies use high resolution data, directly pairing clouds with nearby aerosol properties (Christensen et al., 2017; Bréon et al., 2002). This can be computationally intensive, but allows filtering that can mitigate the influence of confounding variables. A less common method is data assimilation, whereby data products drive a reanalysis model to produce continuous fields of aerosol and cloud properties (Amiri-Farahani et al., 2017; Bellouin et al., 2013). Numerous studies of ACI have used models (recent examples include Neubauer et al., 2017; Gryspeerd et al., 2017).

This report summarises the two sections of the ERACE project to study ACIs using passive imagery. Firstly, products from the Aerosol and Cloud_cci projects are used to calculate various broadband radiation fluxes to quantify the radiative impact of aerosol and cloud. Those are validated against both space and ground-based observations and are then evaluated for trends. Secondly, an extension of Ebmeier et al. (2014) using improved data (and the derived fluxes) and considering a number of different aerosol sources to observe and map ACI. First indirect effects are observed at many sites and the change in cloud albedo is found to vary with aerosol type.

Data

The cloud parameters used in this study are calculated from TOA visible radiances and infrared brightness temperatures in narrow bands centred at 0.55, 0.67, 0.87, 1.6, 3.7, 11, and 12 μm . Aerosol parameters are derived from the first four of those. They were measured by the Along-Track Scanning Radiometers: ATSR-2 operational on the ERS-2 platform from June 1995 to October 2008 and the Advanced ATSR (AATSR), which was operational from March 2002 to April 2012 on the ENVISAT platform. These made two near-

simultaneous views of each pixel at nadir and an inclination of 55° at 10:30 local solar time. Only the nadir view is used for cloud retrievals while both views are used by the aerosol retrieval to separate the signatures of the atmosphere and surface.

The retrievals are performed using the Optimal Retrieval of Aerosol and Cloud (ORAC), an open-source implementation of the optimal estimation method (Rodgers, 2000) to calculate the optical thickness and effective radius of cloud or aerosol particles. It was used because it produces both aerosol and cloud data in a consistent fashion. The version 2.0 cloud retrieval is described in McGarragh et al. (2017) and Stengel et al. (2013). The version 4.01 aerosol retrieval is a new implementation of the algorithm described in Thomas et al. (2009) that uses the Cloud_cci processing chain to retrieve aerosol at full sensor resolution, which is then averaged into 10×10 superpixels.

Broadband fluxes

Methods

Broadband radiative fluxes are computed using BUGSrad (Stephens et al., 2001). BUGSrad is based on the two-stream approximation and correlated- k distribution methods of atmospheric radiative transfer, derived from the algorithm described by Fu and Liou (1992). It is applied to a single-column atmosphere for which the aerosol/cloud layers are assumed to be plane-parallel. Eighteen bands spanning the electromagnetic spectrum are used to compute the broadband flux. Application of this code to satellite data (CloudSat and MODIS) has previously shown excellent agreement with CERES (Clouds and the Earth's Radiant Energy System) measured broadband fluxes (Henderson et al., 2013). Here, a similar strategy is adopted to that study to compute the top and bottom of atmosphere broadband radiative fluxes using the Level 2 ATSR aerosol and cloud optical products. PAR has been extracted from BUGSrad using a similar methodology to that described in Su et al. (2007).

The primary inputs to BUGSrad are the particle effective radius, optical thickness, and solar zenith angle output by an Aerosol_cci product. Vertical profiles of temperature, humidity, and ozone are interpolated from ERA-Interim reanalyses (Dee et al., 2011). Total solar irradiance measurements from the SOHO (Solar and Heliospheric Observatory) and SORCE (SOlar Radiation and Climate Experiment) instruments are gap-filled and homogenised using the method described in Loeb et al. (2008). Constant concentrations are assumed for the well-mixed gases: $\text{CH}_4 = 1.8$ ppm, $\text{N}_2\text{O} = 0.26$ ppm, and $\text{CO}_2 = 380$ ppm. The visible and infrared surface albedo are assumed to be independent of wavelength. Cloud base height is calculated as described in Meerkötter and Zinner (2007) from the cloud top height, optical depth, and effective radius (from the Cloud_cci product) by assuming a semi-adiabatic profile. A pixel is deemed to be overcast or clear when the properties of the cloud or aerosol are used, respectively. Radiative fluxes are calculated twice: once using ingested aerosol/cloud properties and again assuming the pixel is aerosol/cloud free to calculate the aerosol/cloud radiative effect.

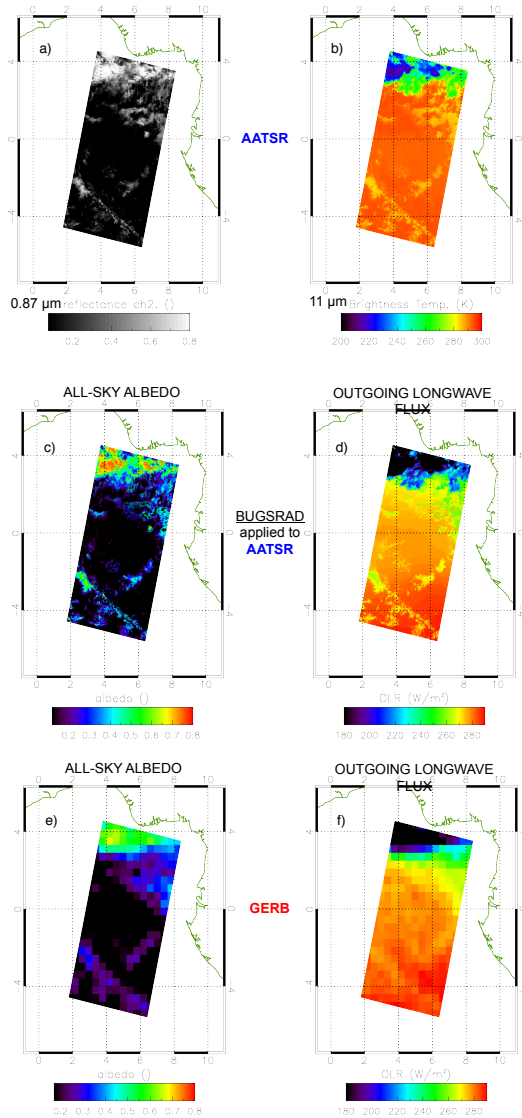


Figure 1: AATSR observations over the Gulf of Guinea on 20 June 2008 showing the (a) $0.87 \mu\text{m}$ reflectance and (b) $11 \mu\text{m}$ brightness temperature. The (c) all-sky albedo and (d) outgoing longwave flux at TOA calculated using BUGSrad compare favourably to collocated observations from GERB (e and f, respectively).

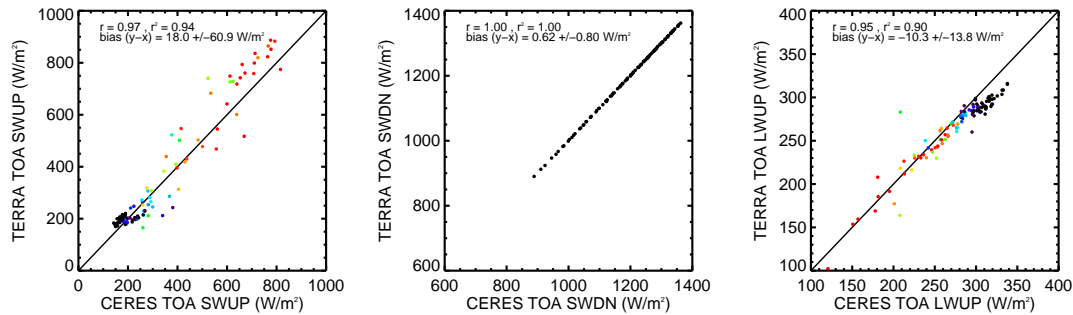


Figure 2: TOA (a) shortwave upwelling, (b) shortwave downwelling, and (c) longwave upwelling fluxes calculated by BUGSrad from the ORAC MODIS Terra product compared to the CERES product over the SAFARI field site. Point colour indicates the cloud fraction from 0 % (black) to 100 % (red), highlighting different biases in the presence of low cloud fractions. Results of a linear regression fit are detailed at the top of each plot.

Validation

Initial validation of the top of atmosphere fluxes was performed by comparison to the ARG (Average Rectified Geolocated) product from the broadband radiometer GERB (Geostationary Earth Radiation Budget) on MSG-2 (Meteosat Second Generation). This is collocated with AATSR, though the two observations are separated by about eight minutes. Fig. 1 shows a granule containing three key conditions: 1) deep convective clouds with low brightness temperature in the north, 2) clear-sky in the middle, and 3) patchy cumulus in the south. The spatial pattern of radiative flux is consistent between the products in all three conditions (accounting for their different spatial resolutions) and potentially provides a more useful representation of the flux from cirrus clouds. Examined in detail, differences in OLR are less than 3 Wm^{-2} , which is acceptable as the uncertainty on the GERB-measured OLR is 1 % and typical OLR values are of order 300 Wm^{-2} (Clerbaux et al., 2009). Bias in the all-sky albedo is much larger ($\sim 13\%$) and outside of GERB's measurement uncertainty. Upwelling fluxes are highly correlated with equivalent values derived from CERES observations (not shown), but with biases in excess of the expected uncertainty. The discrepancy is most pronounced for pixels with a low cloud fraction. This implies that it may have been inappropriate to assume that the surface albedo is constant in all bands.

The broadband algorithm was revised to more accurately represent the surface. The white and black sky albedos were estimated from the MODIS MCD43 product (Wanner et al., 1997), interpolating to the six shortwave bands used in BUGSrad. Thermal emissivity was interpolated from the University of Wisconsin (Madison) baseline fit global emissivity database (Seemann et al., 2008). Fig. 2 repeats the comparison to CERES. The shortwave upwelling flux is now satisfactory for low cloud fractions (black and blue points), but the overall bias was not greatly reduced. In the longwave, the bias increased slightly and it continues to underestimate the flux in low cloud fraction conditions. This may be an inherent problem in the BUGSrad Rayleigh scattering code. The longwave bias again increases when the surface emissivity is included, implying a bias in the skin temperature estimated from ERA-Interim.

Though the broadband fluxes calculated by BUGSrad are biased, they are highly correlated with independent observations and provide a higher spatial resolution than existing products, providing an improved ability to identify the radiative effect of specific aerosol and cloud features. Further validation against in situ data revealed that use of the ORAC retrieved surface temperature reduced the biases. This shouldn't be surprising, as the retrieved surface temperature is radiatively consistent with the other properties, but there is some hesitation to its systematic use as that temperature is neither validated nor designed for scientific application.

Results

Radiative effect is the difference between the observed flux and that expected from a clear-sky atmosphere (i.e. without cloud or aerosols) and is important to quantify for aerosol and cloud because of their strong influence on climate and climate change. Fig. 3 shows the global distributions of cloud radiative effects over the summer months of 2008. The observed net global cloud radiative effect of $-24.7 \pm 2.5 \text{ Wm}^{-2}$ is in agreement with the range of -16.7 to -24.5 Wm^{-2} found by Loeb et al. (2008) while the radiative fluxes are consistent between AATSR-BUGSrad and GERB in clear-sky conditions. Quantitative values estimated from aerosol

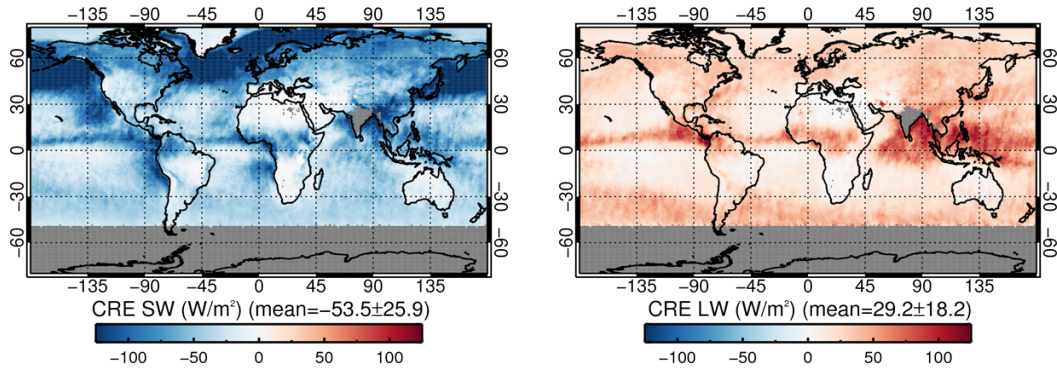


Figure 3: Cloud radiative effect, the difference in outgoing TOA broadband radiation between clear- and all-sky conditions, in the short (left) and longwave (right). Global mean values and standard deviations (weighted by latitude) are provided in brackets and are in agreement with the net value observed by CERES.

and cloud radiative effects agree with past studies (e.g. Ramanathan et al., 1989; Thomas et al., 2013). The spatial pattern of CRE in Fig. 3 is physically reasonable, with large negative forcings in the stratocumulus regions off the west coasts of the US and Peru and strong positive forcings in the monsoon-dominated regions of southeast Asia.

The entirety of the AATSR data record was processed such that changes in CRE could be investigated with a linear trend analysis, shown in Fig. 4. In the shortwave, the strong negative trends above 60° N may result from the reduction in Arctic sea ice extent, while there are signs of marine stratus brightening off the western coast of the US. The cause of the strong positive trend in the Southern Ocean is unclear, but may be related to increased sea ice extent. The influence of El Niño is clear in the longwave trend from the distinctive 'V' pattern over the equatorial Pacific (corresponding to the movement of the Pacific warm pool towards Chile). Increasing cloud top height is also evident off the coast of the African biomass burning region, though this is not expected to be related to aerosol invigoration as these are not predominately convective clouds.

Impact of localised aerosol sources

The second part of this project revises and extends the work presented in Ebmeier et al. (2014) (which will hereafter be referred to as E14). Such averaging over time usually isn't appropriate because aerosol properties will vary significantly with the type of particle and change rapidly in response to removal processes. Hence, the analysis is restricted to regions where a single type of particle is emitted continuously. There, aerosol properties are expected to be a function of time since the particles were emitted, which corresponds to a distance from the source along the wind vector. Hence, rotating data to align with the wind direction should collate observations in similar aerosol conditions. Data upwind will sample ambient conditions while downwind is perturbed by emission, providing a range of aerosol environments with which to map ACIs. To minimise the influence of the surface, averages are made at a similar resolution to the satellite data (1 × 1 km).

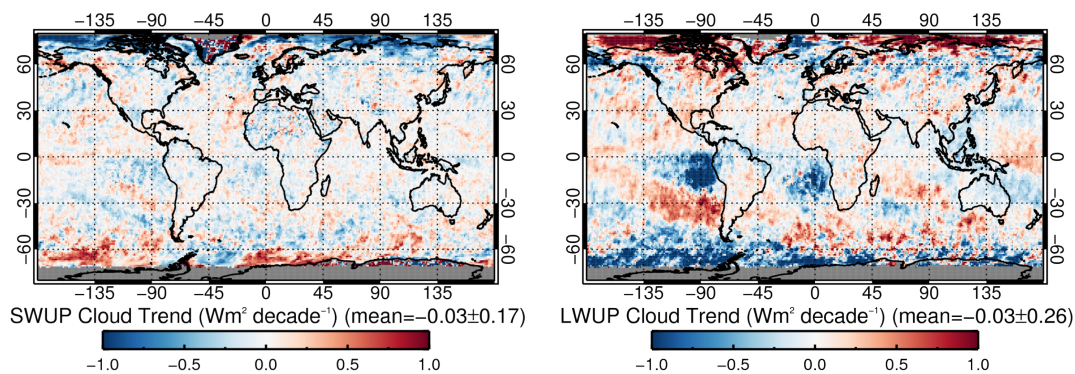


Figure 4: Decadal (linear) trend in (a) short and (b) longwave upwelling flux over the AATSR record (2002–2012). In the longwave, note the influence of El Niño from the characteristic 'V' shape off the Peruvian coast.

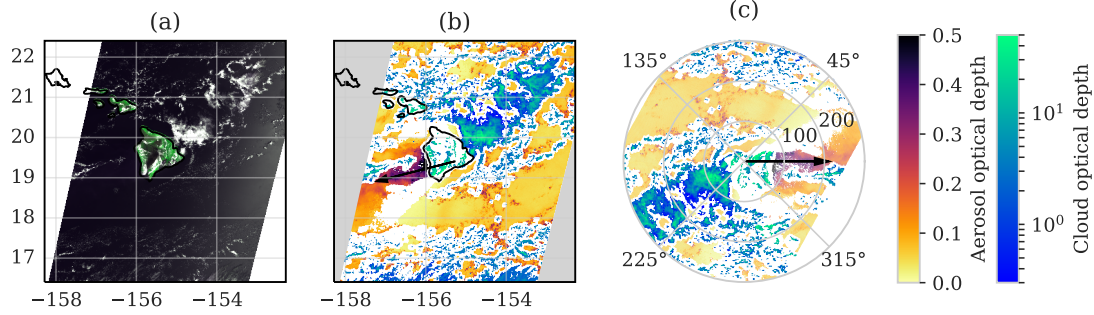


Figure 5: An application of the rotation technique to a scene over Hawaii on 9 Sep 2008. (a) False-colour image from AATSR (Red = 670 nm, Green = 870 nm, Blue = 550 nm). (b) Aerosol optical depth (orange-red) and cloud optical depth (blue-green) retrieved by ORAC from that data. White indicates data removed by quality control (mostly clear sky within 7 km of a cloud). The wind direction reported at Mt. Kilauea by ECMWF data is indicated by an arrow. (c) The same data after mapping onto the wind-corrected grid, centred on the summit with wind blowing from left to right.

Methods

Figure 5 illustrates the action of the rotation technique on a plume of aerosol emitted from Mt. Kilauea, Hawaii. The left panel shows a false-colour image observed by AATSR. The aerosol and cloud properties retrieved by ORAC from that image are shown in the centre panel, with an arrow indicating the wind direction at the summit. The right panel shows the same data after rotation. That is added to a running mean, eventually combining several years of observations into a single rotated image. ACI are expected to appear as a change in the average cloud properties as the aerosol index changes downwind of the source.

Rotation is a standard image processing technique. This study used the openCV library (open source computer vision, <http://opencv.org>). Using a nearest-neighbour library routine, a segment of the swath is mapped to polar coordinates centred on the source. A rotation is made by ‘rolling’ the angular dimension of the result (i.e. one ‘roll’ of the sequence [1,2,3,4] gives [4,1,2,3]). This mapping is only approximate as the size of a satellite pixel is not constant across the swath and the image is a projection onto a sphere while the library treats it as flat. However, it has been found to be reasonably accurate while being fast and providing continuous coverage. The maximum radius considered is 300 km, comparable to the 512 km width of the AATSR swath. The position of the site is converted to a column and row in the swath (c_v, r_v) by using a quadratic fit. Errors in that process are believed to be small as 25 km perturbations in the position produce insignificant changes in the averaged fields.

The wind direction is calculated from the European Centre for Mid-range Weather Forecasting (ECMWF) interim reanalyses (ERA-Interim, Dee et al., 2011). As catalogued at the Centre for Environmental Data Analysis (ECMWF, 2014), the 10 m wind components (zonal u and meridional v) are reported on a reduced Gaussian grid ($\sim 0.7^\circ \times 0.7^\circ$) every six hours. These are bi-linearly interpolated in space to each location and then linearly interpolated to the time of the satellite overpass. The wind direction is $\tan^{-1}(v/u)$. That is translated onto the polar grid by finding the position 0.1° away from the site in the direction of the wind. The coordinates of that point in the swath (c_w, r_w) are found as for the site itself. The rotation required to orient the image with the wind direction is then $\theta = \tan^{-1}[(r_w - r_v)/(c_w - c_v)]$.

E14 used the wind field at the height of the volcano summit while this study uses the surface wind field. This was changed because the effective injection height for non-volcanic sources is unknown. The analysis was repeated for two sites using the wind at various heights through the planetary boundary layer, finding very similar results, so this is not considered a significant source or error.

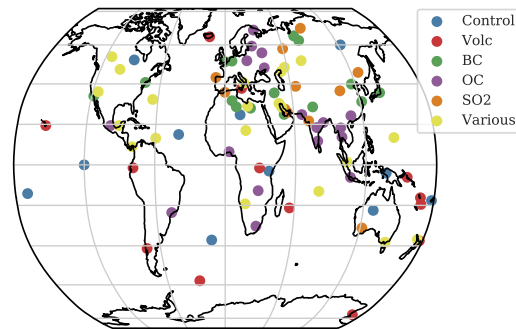


Figure 6: Map of all sites considered in this study. Colour denotes the dominant type of aerosol, as determined by the CMIP6 anthropogenic emissions database. ('Various' indicates that no one aerosol type is dominant.)

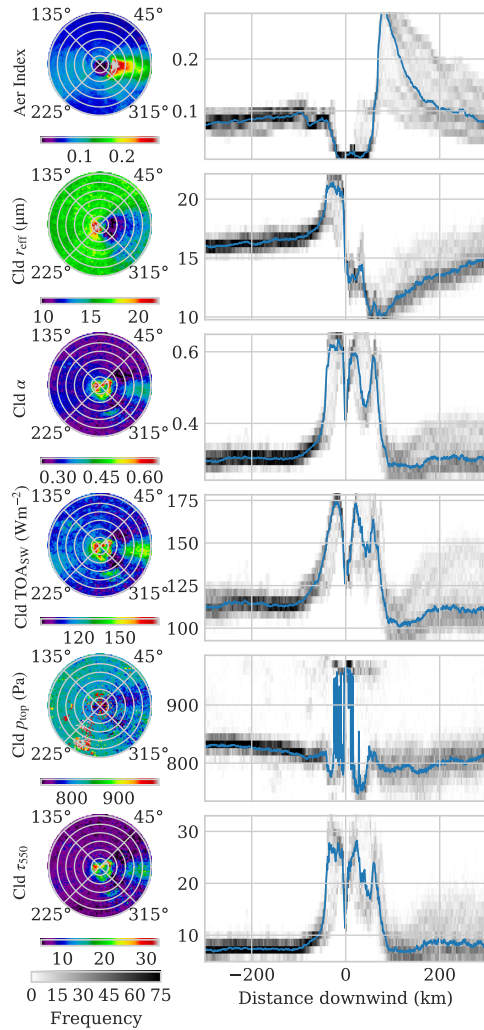


Figure 7: Variation around Mt. Kilauea of (top to bottom) aerosol index, cloud effective radius, cloud albedo at 550 nm, top-of-atmosphere shortwave upwelling radiation, cloud top pressure, and cloud optical depth averaged over the complete AATSR mission. For brevity, all eight meteorological conditions are combined. In the polar plots (left), the summit is at the origin and the wind blows from left to right. Histograms (right) show the distribution as a function of distance from the summit, overplotting the median.

(5) 9 locations at the authors' discretion that sampled regions of the world otherwise neglected (e.g. the Sandwich Isles were highlighted by Gassó (2008)); and

(6) 11 controls where there is no obvious emission source, including the 3 non-volcanic islands evaluated in E14.

The sites in groups 1-4 are selections from a much larger population due to limited computer storage. This subset was selected by visual inspection using Google Earth with the aim to sample a variety of land surfaces, types of emission, and regions of the world. Coordinates were centred on the largest industrial complex within the highlighted region or, in their absence, the centre of the region. The CMIP6 database was used to classify the dominant type of aerosol emitted at each site.

To be clear, this analysis was not expected to work at every single site as the selection criteria were purposefully vague. This was, in part, because the most robust means to determine if an aerosol source is dominant is to use the analysis itself. As such, the 89 sites were not changed once the study began.

The Aerosol_cci dataset averaged the 1 km ORAC retrievals into 10 km superpixels. Only the lower resolution data is presented here for practical reasons, re-sampling the 10 km cells to 1 km using the Cloud_cci mask. Aerosol_cci post-processing counted the number of cloudy pixels within the 3×3 area centred on each aerosol retrieval and rejected any retrievals adjacent to more than 3 cloudy pixels. In light of Christensen et al. (2017) finding that contamination extends about 15 km from the edge of a cloud, this study used a 15×15 box instead, providing a compromise between maximising coverage and minimising pixels where neither retrieval is reliable (the white area of fig. 5b).

Before averaging, each pixel is classified by one of eight conditions. Land and sea are separated as ORAC uses different models for land and sea surfaces, which suffer different errors. Relative humidity and lower tropospheric stability have been shown to strongly constrain the interaction of aerosol and cloud (Chen et al., 2014). A pixel is classified as wet if the free tropospheric humidity is greater than 40 % and dry otherwise while it is classified as stable if the lower tropospheric stability is less than 17°C and unstable otherwise. The latter two definitions follow Neubauer et al. (2017) and the values are interpolated from ECMWF data onto the satellite swath within ORAC.

The rotated images are combined through a running mean (Finch, 2009), giving the mean, variance, and number of data in each rotated bin at 89 sites around the globe, while cloud top pressure (CTP) and the LW and SW upwelling radiance were averaged at a subset of these. The sites, mapped in Fig. 6, are:

(1) 24 sites of significant emissions, evaluated using the CMIP6 (coupled model intercomparison project) anthropogenic emissions estimates for 2000-2014 (Hoesly et al., 2017). Organic carbon, black carbon, and sulphur dioxide emissions were combined and searched for bins with an unusually large mean;

(2) 19 sites of frequent flaring activity, determined by using the World Fire Atlas (Arino et al., 2012) to count the occurrence of hot-spots in 0.05° bins;

(3) 11 volcanoes that were labelled as significant emitters of SO_2 in Carn et al. (2017), had a significant eruption during the AATSR mission, or were evaluated in E14;

(4) 15 of the world's most populous cities;

Further, some sites were selected specifically to test the limitations of the technique: the controls lack an aerosol source; ‘Hamborn’ is within a highly industrialised area with numerous sources; ‘Rural China’ is a crop-burning area where emissions will be seasonal; and ‘Erebus’ is in darkness for several months of the year.

Results

The Kilauea volcano in Hawaii is one of the most significant natural sources of SO_2 (Carn et al., 2017). Its plume can clearly be seen in most satellite aerosol products over the relatively clean oceanic background. E14 observed a first indirect effect downwind of Kilauea well outside of natural variation, making it an obvious candidate for an initial investigation.

Figure 7 shows full-mission averages there for each variable evaluated. There is little variation upwind while the plume is obvious downwind. The plume is relatively narrow, producing broad histograms downwind as they sample both clean and polluted air. AI increases from 0.1 to 0.15–0.25 while CER decreases from 16 to 10–15 μm , an unambiguous first indirect effect of similar magnitude to that observed in E14. Cloud albedo is enhanced by up to 0.1 with a corresponding increase in upwelling SW radiation, though these are constrained to the core of the aerosol plume. A decrease in cloud top pressure hints at cloud invigoration, but that should be viewed with scepticism as it continues a trend seen in the upwind data. Examining the full field, there is a general decrease in CTP downwind, corresponding to a drop in lower tropospheric stability, that is restored in the presence of aerosol. However, COD also increases downwind, which may imply an increase in the LWP. The large variations near the origin relate to discontinuities between retrievals over land and sea.

The functional form of CAI in this region is estimated by producing two-dimensional histograms of each cloud property against AI, as shown in Fig. 8. This treated each pixel in the rotated field as an independent datum. Pixels which averaged fewer than 10 observations (which corresponds to less than one observation per year) were removed as outliers. Bins which represented less than 1% of the total area (either by containing few bins or many bins near the origin) are not plotted for clarity. As a simple model of the relationships, an orthogonal-distance regression to all data underlying each histogram was performed, accounting for each pixel’s standard deviation in both variables. If that failed to converge, a standard linear regression was used instead. Note that at Kilauea relatively few observations were obtained in dry conditions or over land.

Firstly, larger AIs are observed in unstable conditions than stable, which may result from increased AOD in the presence of convection. Cloud effective radius and cloud top pressure decrease with increasing AI in unstable conditions but appear to remain constant in stable conditions. This may be because the effects are only detectable at the largest values of AI. Cloud albedo and COD increase at similar rates in both stable and unstable conditions, which implies the change in albedo is dominated by the change in optical thickness rather than the indirect effect. Likely, the threshold chosen to divide dry and humid conditions was inappropriate.

Regardless, the analysis was applied to all 89 sites to estimate the rate of change of cloud effective radius and albedo with log AI. The distribution of these is shown in Fig. 9, flagging each site by the dominant type of aerosol in the AeroCom climatology developed by Stefan Kinne (personal communication, 2017). Sea-salt and organic aerosols show minimal variation in clouds as a function of AI. Dusty regions usually show

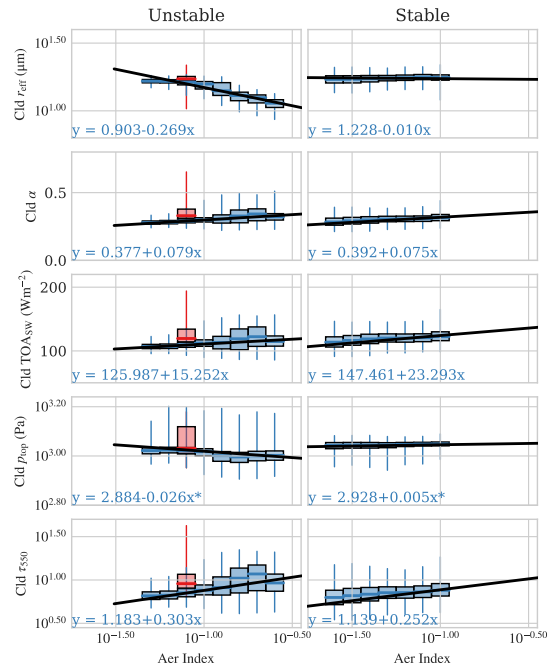


Figure 8: Distributions of the cloud variables shown in Fig. 7 as a function of AI. Boxes show the median and quartiles for 0.1 increments of log AI, with whiskers giving the 1st and 99th percentiles. Bins that contained less than 1% of the total area are excluded. Pixels over land are in red and over sea in blue. Wet, unstable atmospheres are shown to the left and wet, stable to the right. A linear regression to the underlying data is overplotted in black and printed in the bottom corner of each plot. A star denotes data where orthogonal distance regression failed to converge and a simple regression was applied instead.

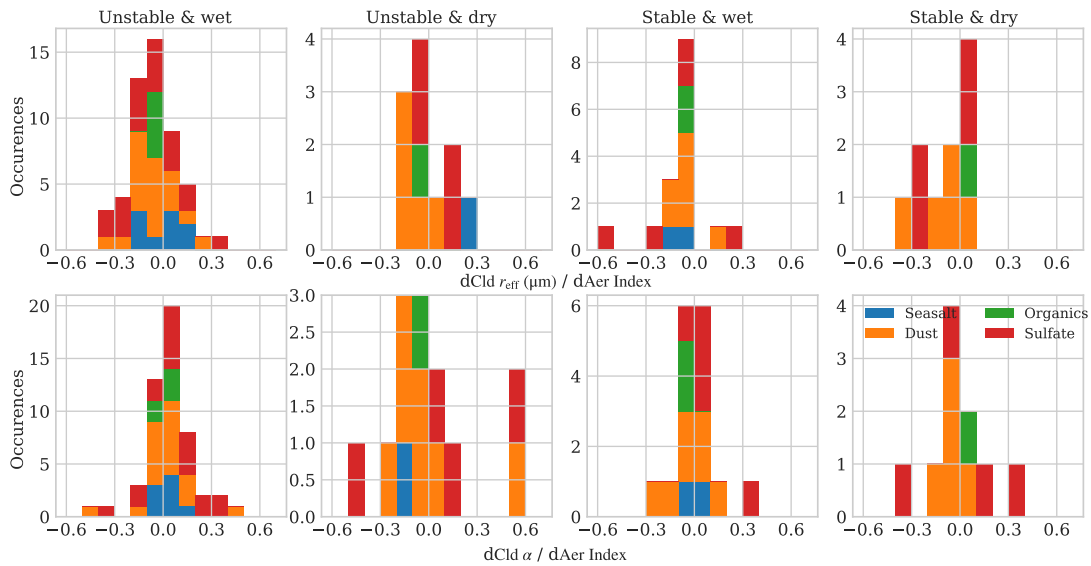


Figure 9: Distribution of the rate of change of cloud effective radius (top) and cloud albedo (bottom) against log AI for the 89 sites considered, classified by the dominant type of aerosol present at that site in the climatology developed for AeroCom by Stefan Kinne (colour). The columns combine land and sea across the four meteorological conditions.

decreases in effective radius but minimal sensitivity to cloud albedo (except in dry conditions, where there is a chance that dust is being mis-classified as cloud, which tends to decrease effective radius as dust particles are smaller than cloud droplets). There is significant variation in the response sulfate aerosols.

Conclusions

The broadband fluxes, though far from perfect, have proven useful in the study of the radiative impact of clouds and aerosols, contributing to the publication of Popp et al. (2016), Christensen et al. (2017), and Sus et al. (2017) and are being used to evaluate the UK Earth System Model. After extensive validation, the remaining biases in these products is believed to results from assumptions in the radiative transfer codes used and the ORAC forward model, making them difficult to reduce further.

The evaluation of ACI from wind-rotated satellite data has produced intriguing, if incomplete, results. Fairly unambiguous signals have been observed at a variety of sites around the globe, but the simplistic wet/dry classification was insufficient to correct for humidity-mediated effects in most circumstances. The analysis will be adjusted to produce multidimensional histograms (rather than means) accounting for the humidity, stability, and liquid water path at each observation. In addition to correcting a few minor bugs, it is hoped that this will separate the influence of meteorology on cloud from the influence of aerosol.

This project contributed to the following presentations:

- October 9–13 2017: AeroCom Conference (Helsinki, Finland);
- July 13–14 2017: Royal Meteorological Society Annual Conference — Weather and Climate Impacts (Exeter, UK);
- March 21–23 2017: International Conference on Aerosol Cycle (Lille, France);
- May 9–13th 2016: Living Planet Symposium (Prague, Czech Republic);
- April 13–15th 2016: ACPC Workshop (Oxford, UK);
- March 21st 2016: NCEO Staff Meeting (Reading, UK);
- October 5–9th 2015: AeroCom Conference (Frascati, Italy);
- June 12th 2015: EOS Seminar (Leicester, UK).

The significant contributions of Matt Christensen to this project are gratefully acknowledged. The ongoing work of Don Grainger, Greg McGarragh, Caroline Poulsen, Simon Proud, and Gareth Thomas were also instrumental in the project's progress.

References

- Amiri-Farahani, A., Allen, J. R., Neubauer, D., and Lohmann, U. (2017). Impact of Saharan dust on North Atlantic marine stratocumulus clouds: Importance of the semidirect effect. *Atmospheric Chemistry and Physics*, 17(10):6305–6322, doi:10.5194/acp-17-6305-2017.
- Anderson, T. L., Charlson, R. J., Winker, D. M., Ogren, J. A., and Holmén, K. (2003). Mesoscale Variations of Tropospheric Aerosols. *Journal of the Atmospheric Sciences*, 60(1):119–136, doi:10.1175/1520-0469(2003)060<0119:MVOTA>2.0.CO;2.
- Arino, O., Casadio, S., and Serpe, D. (2012). Global night-time fire season timing and fire count trends using the ATSR instrument series. *Remote Sensing of Environment*, 116:226–238, doi:10.1016/j.rse.2011.05.025.
- Bellouin, N., Quaas, J., Morcrette, J. J., and Boucher, O. (2013). Estimates of aerosol radiative forcing from the MACC re-analysis. *Atmospheric Chemistry and Physics*, 13(4):2045–2062, doi:10.5194/acp-13-2045-2013.
- Bréon, F.-M., Tanré, D., and Generoso, S. (2002). Aerosol effect on cloud droplet size monitored from satellite. *Science*, 295(5556):834–8, doi:10.1126/science.1066434.
- Carn, S. A., Fioletov, V. E., McLinden, C. A., Li, C., and Krotkov, N. A. (2017). A decade of global volcanic SO₂ emissions measured from space. *Scientific Reports*, 7:44095, doi:10.1038/srep44095.
- Chen, Y.-C., Christensen, M. W., Stephens, G. L., and Seinfeld, J. H. (2014). Satellite-based estimate of global aerosol-cloud radiative forcing by marine warm clouds. *Nature Geoscience*, 7(9):643–646, doi:10.1038/ngeo2214.
- Christensen, M. W., Chen, Y. C., and Stephens, G. L. (2016). Aerosol indirect effect dictated by liquid clouds. *Journal of Geophysical Research — Atmospheres*, 121(24):14636–14650, doi:10.1002/2016JD025245.
- Christensen, M. W., Neubauer, D., Poulsen, C., Thomas, G., McGarragh, G., Povey, A. C., Proud, S., and Grainger, R. G. (2017). Unveiling aerosol-cloud interactions Part 1: Cloud contamination in satellite products enhances the aerosol indirect forcing estimate. *Atmospheric Chemistry and Physics*, 17(Nov):13151–13164, doi:10.5194/acp-17-13151-2017.
- Clerbaux, N., Russell, J., Dewitte, S., Bertrand, C., Caprion, D., De Paepe, B., Gonzalez Sotelino, L., Ipe, A., Bantges, R., and Brindley, H. (2009). Comparison of GERB instantaneous radiance and flux products with CERES Edition-2 data. *Remote Sensing of Environment*, 113(1):102–114, doi:10.1016/j.rse.2008.08.016.
- Dee, D. P., Uppala, S. M., Simmons, A. J., Berrisford, P., Poli, P., Kobayashi, S., Andrae, U., Balmaseda, M. A., Balsamo, G., Bauer, P., Bechtold, P., Beljaars, A. C. M., van de Berg, L., Bidlot, J., Bormann, N., Delsol, C., Dragani, R., Fuentes, M., Geer, A. J., Haimberger, L., Healy, S. B., Hersbach, H., Hólm, E. V., Isaksen, I., Kållberg, P., Köhler, M., Matricardi, M., McNally, A. P., Monge-Sanz, B. M., Morcrette, J. J., Park, B. K., Peubey, C., de Rosnay, P., Tavolato, C., Thépaut, J. N., and Vitart, F. (2011). The ERA-Interim reanalysis: Configuration and performance of the data assimilation system. *Quarterly Journal of the Royal Meteorological Society*, 137(656):553–597, doi:10.1002/qj.828.
- Dines, W. H. (1917). The heat balance of the atmosphere. *Quarterly Journal of the Royal Meteorological Society*, 43(182):151–158, doi:10.1002/qj.49704318203.
- Ebmeier, S. K., Sayer, A. M., Grainger, R. G., Mather, T. A., and Carboni, E. (2014). Systematic satellite observations of the impact of aerosols from passive volcanic degassing on local cloud properties. *Atmospheric Chemistry and Physics*, 14(19):10601–10618, doi:10.5194/acp-14-10601-2014.
- ECMWF (2014). ECMWF ERA-Interim: reduced N256 Gaussian gridded surface level analysis time parameter data (ggas). NCAS British Atmospheric Data Centre. <http://catalogue.ceda.ac.uk/uuid/3075228bcb09e90bf3717f9eeb0fed5b>.
- Finch, T. (2009). Incremental calculation of weighted mean and variance. Technical report, University of Cambridge Computing Service. <http://people.ds.cam.ac.uk/fanf2/hermes/doc/antiforgery/stats.pdf>.
- Fu, Q. and Liou, K. N. (1992). On the correlated k-distribution method for radiative transfer in nonhomogeneous atmospheres. *Journal of the Atmospheric Sciences*, 49(22):2139–2156, doi:10.1175/1520-0469(1992)049<2139:OTCDMF>2.0.CO;2.
- Gassó, S. (2008). Satellite observations of the impact of weak volcanic activity on marine clouds. *Journal of Geophysical Research — Atmospheres*, 113:D14S19, doi:10.1029/2007JD009106.
- Grandey, B. S. and Stier, P. (2010). A critical look at spatial scale choices in satellite-based aerosol indirect effect studies. *Atmospheric Chemistry and Physics*, 10(2009):11459–11470, doi:10.5194/acp-10-11459-2010.
- Gryspeerdt, E., Quaas, J., Ferrachat, S., Gettelman, A., Ghan, S., Lohmann, U., Morrison, H., Neubauer, D., Partridge, D. G., Stier, P., Takemura, T., Wang, H., Wang, M., and Zhang, K. (2017). Constraining the instantaneous aerosol influence on cloud albedo. *Proceedings of the National Academy of Sciences*, 114(19):201617765, doi:10.1073/pnas.1617765114.
- Gryspeerdt, E., Stier, P., and Grandey, B. S. (2014). Cloud fraction mediates the aerosol optical depth-cloud top height relationship. *Geophysical Research Letters*, 41(10):3622–3627, doi:10.1002/2014GL059524.
- Haywood, J. M. and Shine, K. P. (1995). The effect of anthropogenic sulfate and soot aerosol on the clear-sky planetary radiation budget. *Geophysical Research Letters*, 22(5):603–606, doi:10.1029/95gl00075.
- Henderson, D. S., L'Ecuyer, T., Stephens, G., Partain, P., and Sekiguchi, M. (2013). A Multisensor Perspective on the Radiative Impacts of Clouds and Aerosols. *Journal of Applied Meteorology and Climatology*, 52:853–871, doi:10.1175/JAMC-D-12-025.1.
- Hoesly, R. M., Smith, S. J., Feng, L., Klimont, Z., Janssens-Maenhout, G., Pitkanen, T., Seibert, J. J., Vu, L., Andres, R. J., Bolt, R. M., Bond, T. C., Dawidowski, L., Kholod, N., Kurokawa, J.-I., Li, M., Liu, L., Lu, Z., Moura, M. C. P., O'Rourke, P. R., and Zhang, Q. (2017). Historical (1750–2014) anthropogenic emissions of reactive gases and aerosols from the community emission data system (ceds). *Geoscientific Model Development Discussions*, 2017:1–41, doi:10.5194/gmd-2017-43.
- IPCC (2014). *Climate Change 2014: Impacts, Adaptation, and Vulnerability. Part A: Global and Sectoral Aspects. Contribution of Working Group II to the Fifth Assessment Report of the Intergovernmental Panel on Climate Change*. Cambridge University Press, New York. [Field, C.B., V.R. Barros, D.J. Dokken, K.J. Mach, M.D. Mastrandrea, T.E. Bilir, M. Chatterjee, K.L. Ebi, Y.O. Estrada, R.C. Genova, B. Girma, E.S. Kissel, A.N. Levy, S. MacCracken, P.R. Mastrandrea, and L.L. White (eds.)].

- Liu, J. and Li, Z. (2014). Estimation of cloud condensation nuclei concentration from aerosol optical quantities: Influential factors and uncertainties. *Atmospheric Chemistry and Physics*, 14(1):471–483, doi:10.5194/acp-14-471-2014.
- Loeb, N. G., Wielicki, B. A., Doelling, D. R., Smith, G. L., Keyes, D. F., Kato, S., Manalo-Smith, N., and Wong, T. (2008). Toward optimal closure of the Earth's top-of-atmosphere radiation budget. *Journal of Climate*, 22(3):748–766, doi:10.1175/2008JCLI2637.1.
- Lohmann, U. and Feichter, J. (2005). Global indirect aerosol effects: a review. *Atmospheric Chemistry and Physics*, 5(3):715–737, doi:10.5194/acp-5-715-2005.
- Manabe, S., Strickler, R. F., Manabe, S., and Strickler, R. F. (1964). Thermal Equilibrium of the Atmosphere with a Convective Adjustment. *Journal of the Atmospheric Sciences*, 21(4):361–385, doi:10.1175/1520-0469(1964)021<0361:TEOTAW>2.0.CO;2.
- McComiskey, A. and Feingold, G. (2012). The scale problem in quantifying aerosol indirect effects. *Atmospheric Chemistry and Physics*, 12(2):1031–1049, doi:10.5194/acp-12-1031-2012.
- McGarragh, G., Poulsen, C., Thomas, G., Povey, A., Sus, O., Stapelberg, S., Schlundt, C., Proud, S., Christensen, M., Stengel, M., Hollmann, R., and Grainger, R. (2017). The Community Cloud Retrieval for CLimate (CC4CL). Part II: The optimal estimation approach. *Atmospheric Measurement Techniques*, doi:10.5194/amt-2017-333.
- Meerkötter, R. and Zinner, T. (2007). Satellite remote sensing of cloud base height for convective cloud fields: A case study. *Geophysical Research Letters*, 34(17):L17805, doi:10.1029/2007GL030347.
- Nakajima, T., Higurashi, A., Kawamoto, K., and Penner, J. E. (2001). A possible correlation between satellite-derived cloud and aerosol microphysical parameters. *Geophysical Research Letters*, 28(7):1171–1174, doi:10.1029/2000GL012186.
- Neubauer, D., Christensen, W. M., Poulsen, A. C., and Lohmann, U. (2017). Unveiling aerosol-cloud interactions - Part 2: Minimising the effects of aerosol swelling and wet scavenging in ECHAM6-HAM2 for comparison to satellite data. *Atmospheric Chemistry and Physics*, 17(21):13165–13185, doi:10.5194/acp-17-13165-2017.
- Popp, T., Leeuw, G. D., Bingen, C., Brühl, C., Capelle, V., Chedin, A., Clarisse, L., Dubovik, O., Grainger, R., Griesfeller, J., Heckel, A., Kinne, S., Klüser, L., Kosmale, M., Kolmonen, P., Lelli, L., Litvinov, P., Mei, L., North, P., Pinnock, S., Povey, A., Zweers, D. S., Thomas, G., Tilstra, L. G., and Vandenbussche, S. (2016). Development, Production and Evaluation of Aerosol Climate Data Records from European Satellite Observations (Aerosol_cci). *Remote Sensing*, 8(5):421, doi:10.3390/rs8050421.
- Quaas, J., Boucher, O., Bellouin, N., and Kinne, S. (2008). Satellite-based estimate of the direct and indirect aerosol climate forcing. *Journal of Geophysical Research — Atmospheres*, 113:D05204, doi:10.1029/2007jd008962.
- Ramanathan, V., Cess, R. D., Harrison, E. F., Minnis, P., Barkstrom, B. R., Ahmad, E., and Hartmann, D. (1989). Cloud-Radiative Forcing and Climate: Results from the Earth Radiation Budget Experiment. *Science*, 243(4887):57–63, doi:10.1126/science.243.4887.57.
- Rodgers, C. D. (2000). *Inverse Methods for Atmospheric Sounding: Theory and Practice*, volume 2. World Scientific, Singapore, second edition.
- Rosenfeld, D., Williams, E., Andreae, M. O., Freud, E., Poschl, U., and Rennó, N. O. (2012). The scientific basis for a satellite mission to retrieve CCN concentrations and their impacts on convective clouds. *Atmospheric Measurement Techniques*, 5(8):2039–2055, doi:10.5194/amt-5-2039-2012.
- Seemann, S. W., Borbas, E. E., Knuteson, R. O., Stephenson, G. R., and Huang, H. L. (2008). Development of a global infrared land surface emissivity database for application to clear sky sounding retrievals from multispectral satellite radiance measurements. *Journal of Applied Meteorology and Climatology*, 47(1):108–123, doi:10.1175/2007JAMC1590.1.
- Shinozuka, Y. and Redemann, J. (2011). Horizontal variability of aerosol optical depth observed during the ARCTAS airborne experiment. *Atmospheric Chemistry and Physics*, 11(16):8489–8495, doi:10.5194/acp-11-8489-2011.
- Stengel, M., Mieruch, S., Jerg, M., Karlsson, K.-G., Scheirer, R., Maddux, B., Meirink, J., Poulsen, C., Siddans, R., Walther, A., and Hollmann, R. (2013). The Clouds Climate Change Initiative: Assessment of state-of-the-art cloud property retrieval schemes applied to AVHRR heritage measurements. *Remote Sensing of Environment*, 162:363–379, doi:10.1016/j.rse.2013.10.035.
- Stephens, G. L. (2005). Cloud feedbacks in the climate system: A critical review. *Journal of Climate*, 18(2):237–273, doi:10.1175/JCLI-3243.1.
- Stephens, G. L., Gabriel, P. M., and Partain, P. T. (2001). Parameterization of Atmospheric Radiative Transfer. Part I: Validity of Simple Models. *Journal of the Atmospheric Sciences*, 58(22):3391–3409, doi:10.1175/1520-0469(2001)058<3391:POARTP>2.0.CO;2.
- Stier, P. (2016). Limitations of passive satellite remote sensing to constrain global cloud condensation nuclei. *Atmospheric Chemistry and Physics*, 16(10):6595–6607, doi:10.5194/acp-16-6595-2016.
- Su, W., Charlock, T. P., Rose, F. G., and Rutan, D. (2007). Photosynthetically active radiation from Clouds and the Earth's Radiant Energy System (CERES) products. *Journal of Geophysical Research — Biogeosciences*, 112(G02):022, doi:10.1029/2006JG000290.
- Sus, O., Stengel, M., Stapelberg, S., McGarragh, G. R., Poulsen, C. A., Povey, A. C., Schlundt, C., Thomas, G. E., Christensen, M. W., Proud, S., Jerg, M., Grainger, R. G., and Hollmann, R. (2017). The Community Cloud Retrieval for CLimate (CC4CL). Part I: A framework applied to multiple satellite imaging sensors. *Atmospheric Measurement Techniques*, doi:10.5194/amt-2017-334.
- Thomas, G. E., Chalmers, N., Harris, B., Grainger, R. G., and Highwood, E. J. (2013). Regional and monthly and clear-sky aerosol direct radiative effect (and forcing) derived from the GlobAEROSOL-AATSR satellite aerosol product. *Atmospheric Chemistry and Physics*, 13(1):393–410, doi:10.5194/acp-13-393-2013.
- Thomas, G. E., Poulsen, C. A., Sayer, A. M., Marsh, S. H., Dean, S. M., Carboni, E., Siddans, R., Grainger, R. G., and Lawrence, B. N. (2009). The GRAPE aerosol retrieval algorithm. *Atmospheric Measurement Techniques*, 2(2):679–701, doi:10.5194/amt-2-679-2009.
- Twomey, S. (1967). Pollution and the Planetary Albedo. *Atmospheric Environment*, 8(12):1251–1256, doi:10.1016/j.atmosenv.2007.10.062.
- Twomey, S. (1977). The Influence of Pollution on the Shortwave Albedo of Clouds. *Journal of the Atmospheric Sciences*, 34(7):1149–1152, doi:10.1175/1520-0469(1977)034<1149:TIOPT>2.0.CO;2.
- Wanner, W., Strahler, A. H., Hu, B., Lewis, P., Muller, J.-P., Li, X., Barker Schaaf, C. L., and Barnsley, M. J. (1997). Global retrieval of bidirectional reflectance and albedo over land from EOS MODIS and MISR data: Theory and algorithm. *Journal of Geophysical Research — Atmospheres*, 102(D14):17143–17161, doi:10.1029/96JD03295.